

Tailoring the surface properties of Ti6Al4V by controlled chemical oxidation

Fabio Variola^{a,b}, Ji-Hyun Yi^b, Ludovic Richert^b, James D. Wuest^c,
Federico Rosei^a, Antonio Nanci^{b,*}

^a *Institut National de la Recherche Scientifique-Énergie, Matériaux et Télécommunications, Université du Québec, Varennes, Québec J3X 1S2, Canada*

^b *Laboratory for the Study of Calcified Tissues and Biomaterials, Faculté de Médecine Dentaire,
Université de Montréal, Montréal, Québec H3C 3J7, Canada*

^c *Département de Chimie, Université de Montréal, Montréal, Québec H3C 3J7, Canada*

Received 7 August 2007; accepted 24 November 2007

Available online 26 December 2007

Abstract

Many efforts have been made to promote cell activity at the surface of implants, mainly by modifying their topography and physicochemical properties. Here we demonstrate the feasibility of creating Ti6Al4V surfaces having both a microtexture and a nanotexture, and show that their properties can be tailored by controlling the length of exposure to a mixture of H₂SO₄ and H₂O₂. Scanning electron microscopy (SEM), combined with energy-dispersive X-ray spectroscopy (EDX), indicated that β-phase grains, which surround larger α-phase grains, are etched more rapidly, resulting in a surface composed of microscale cavities with α-grain boundaries. Furthermore, high-resolution SEM and atomic force microscopy (AFM) revealed the presence on the surfaces of both α- and β-phase grains of a network of nanopits with mean diameters ranging between 13 and 21 nm. The grain surface roughness increases from about 4 nm on untreated samples to about 12 nm after 4 h of treatment. AFM analysis showed that the depth of microscale cavities can be varied in the 10–180 nm range by controlling the extent of chemical etching. Fourier transform infrared spectroscopy (FT-IR), combined with ellipsometry, established that the etching generated an oxide layer with a thickness in the range 15–45 nm. The resulting new surfaces selectively promote the growth of osteoblasts while inhibiting that of fibroblasts, making them promising tools for regulating the activities of cells in biological environments.

© 2007 Elsevier Ltd. All rights reserved.

Keywords: Bioactivity; Cell proliferation; Nanotopography; Surface modification; Titanium alloy; Titanium oxide

1. Introduction

Titanium and its alloys are widely used in dentistry and orthopedics for their mechanical properties, high strength-to-weight ratio, exceptional biocompatibility, and high corrosion resistance. An important feature of Ti-based materials is their air-induced passivation, which creates a protective and stable layer of titanium oxide on the surface. The native oxide is normally thin (usually in the 3–10 nm range), amorphous, and stoichiometrically defective [1–5]. The stability of the oxide layer depends on its chemical composition,

crystalline structure, and thickness, characteristics that can all be modulated by appropriate surface treatment.

Interactions between biomaterials and biological environments occur at interfaces, and they are affected by the nature of the biomaterial, such as its surface chemistry and energy, roughness, and topography [6]. It is generally accepted that rough and porous surfaces have a more pronounced and beneficial influence on cellular activity than smooth ones. Many methods have been used to modify surfaces to enhance tissue repair events, such as sand-blasting [7–9], machining [10–12], anodization [13,14], lithography [15–17], ion-implantation [18–21], and chemical etching [22–24]. However, many of the surface modifications introduced by such treatments generate microscale features. Consequently, most studies so far have

* Corresponding author. Tel.: +1 514 343 5846; fax: +1 514 343 2233.

E-mail address: antonio.nanci@umontreal.ca (A. Nanci).

focused on how microscale features affect cellular activities (including adhesion, proliferation, differentiation, and gene expression [1,22,25–27]), as well as protein adsorption [28]. Microscale features are generally believed to achieve their effect by creating microenvironments that have secondary impacts on cell recruitment and function. However, cellular events such as interactions with substrates and cell signaling takes place on the nanoscale, suggesting that efficient topographical cueing should also operate on this scale. Indeed, recent studies have shown that nanometric cues can significantly influence cell activities, including stimulating the differentiation of stem cells derived from bone marrow along the osteogenic pathway [15]. The ability of nanofeatures to directly influence cell activity offers the potential to develop a novel generation of implantable biomaterials that can improve interactions with the host tissue [29–34].

To understand how physical nanostructures affect cellular phenomena, different techniques have been developed for creating ordered and unordered surface nanotopographies, such as photolithography and electron-beam lithography [35–37], polymer demixing [38], and phase separation [39]. In addition, we have demonstrated that a network of nanopits can be created on commercially pure Ti by etching for 2 h with an aqueous mixture of H_2SO_4 and H_2O_2 (piranha solution) [30,40]. The resulting nanoporosity has beneficial effects on both short-term and long-term osteogenic events *in vitro* [41,42]. This oxidative treatment is also effective on Ti6Al4V alloy, and the newly generated surface upregulates the expression of certain bone matrix protein by cultured osteogenic cells [41]. However, it is still not known if treatment time can affect the morphological and physicochemical characteristics of the nanoporous surface created by this chemical oxidative patterning.

Therefore, the main objective of the present study was to determine if treatment time can be used to control the physicochemical characteristics of nanopitted surfaces on Ti6Al4V alloy. Cell culture was used to probe the influence of the surfaces on fibroblastic and osteogenic cell adhesion and growth. Our results show that surface features such as topography, roughness, and physicochemical properties can be controlled by varying the extent of chemical oxidation. They also indicate that the changes induced by treatment operate collectively to generate surfaces with selective influence on cell growth; in particular, they uniquely promote the growth of osteogenic cells and limit that of fibroblastic cells. Such a capacity for selective cell influence is expected to accelerate the healing process at implantation sites and to improve tissue integration.

2. Materials and methods

2.1. Controlled chemical oxidation of Ti6Al4V disks

Ti6Al4V disks, 12 mm in diameter and 2 mm in thickness (Titanium Industries, Montréal, Québec, Canada), were mechanically polished to a mirror finish (PowerPro5000™, Buehler, Lake Bluff, USA) by using SiC grinding paper, then diamond paste, and finally a suspension of SiO_2 . The polished disks were then cleaned with toluene in an ultrasonic bath for 20 min (Fisher Scientific, Fair Lawn, NJ) and finally dried in air.

The piranha solution used for etching was prepared by carefully adding pure (95–97%, equivalent to 36 N) H_2SO_4 (J.T. Baker, Phillipsburg, NJ) to an equal volume of 30% aqueous H_2O_2 (Fisher Scientific). Freshly prepared solutions were cooled briefly in ice to reduce their temperature to 22 °C, and then polished Ti-alloy disks were immersed in them. Etching was arrested at set intervals by adding distilled water after 15 min, 30 min, 1 h, 2 h, and 4 h, thereby defining five different conditions for physicochemical analysis (plus the original untreated polished discs as controls). After etching was stopped, the recovered disks were rinsed with distilled water, washed further with ethanol in an ultrasonic bath for 20 min, and subsequently dried in air, according to a previously established protocol [30]. Untreated polished disks used as controls were cleaned with ethanol for 20 min in the ultrasonic bath and dried in air. Each etching experiment was repeated six times.

2.2. Structural analysis

Surfaces of etched disks and untreated controls were examined by using a JEOL-JSM7400F field-emission scanning electron microscope (SEM). Images were processed by analySIS[®] software (Soft Imaging System GmbH, Münster, Germany) to determine the evolution of the mean pit diameter with increasing etching time. Energy-dispersive X-ray analysis was performed by using the INCA Energy system (Oxford Instruments Analytical, Bucks, England) to assay differences in composition and preferential chemical attack on particular phases. Backscattered electron images were obtained using a JEOL JSM-6460LV variable-pressure SEM (LV-SEM) operating at 15 kV to visualize the distribution of phases. Variations in surface topography on the nanoscale were characterized by atomic force microscopy (AFM) in tapping mode using a JEOL JSPM-5200 instrument.

2.3. X-ray diffraction (XRD)

To assess whether the chemical treatment changed the amorphous nature of the native oxide layer, treated samples were investigated by using a Philips PANalytical X'Pert Pro diffractometer equipped with a secondary monochromator (Cu K α radiation, $\lambda = 0.15405$ nm) in grazing incidence mode. The incident beam angle ω was 0.5° and the range of 2θ was 20–85°.

2.4. Spectroscopic analysis

2.4.1. X-ray photoelectron spectroscopy (XPS)

Information about the chemical composition of the surfaces of etched discs and controls was obtained by using an ESCALAB 220I-XL spectrophotometer equipped with an Al K α (1486.6 eV) monochromatic source at base pressures less than 10^{-8} Torr with a perpendicular take-off angle. High-resolution spectra were charge-compensated by setting the binding energy of the C_{1s} peak to 284.6 eV. Peaks were fitted (Gaussian/Lorentzian curves) after background subtraction (Shirley type) with CasaXPS[®] software (Casa Software Ltd), taking in consideration Scofield sensitivity factors [43]. Depth profiles were obtained with 3 keV Argon sputtering focused on a 2.25 mm² area on a sample etched for 4 h. C_{1s} and Ti_{2p} peaks were considered for this analysis. In order to reduce peak shift due to charge accumulation, peak positions were adjusted by using the Ar peak (242.4 eV) as reference [43].

2.4.2. Fourier transform infrared spectroscopy (FT-IR)

Infrared spectroscopy was used to probe the modified oxide layer resulting from controlled chemical oxidation. A Nexus 870 FT-IR spectrometer equipped with a SAGA (smart aperture grazing-angle) accessory (Thermo Nicolet, Madison, WI) was used. Analysis of the thin oxide layer was performed in grazing-angle mode at an angle of 80° with respect to the surface normal, using a spectral resolution of 4 cm⁻¹ in the 475–4000 cm⁻¹ range. Spectroscopic information was collected from an 8 mm diameter area. A gold substrate was used to collect a background spectrum. Spectra were finally fitted by PeakFit software (SPSS, Chicago, IL) using Pearson VII functions as reported previously [40].

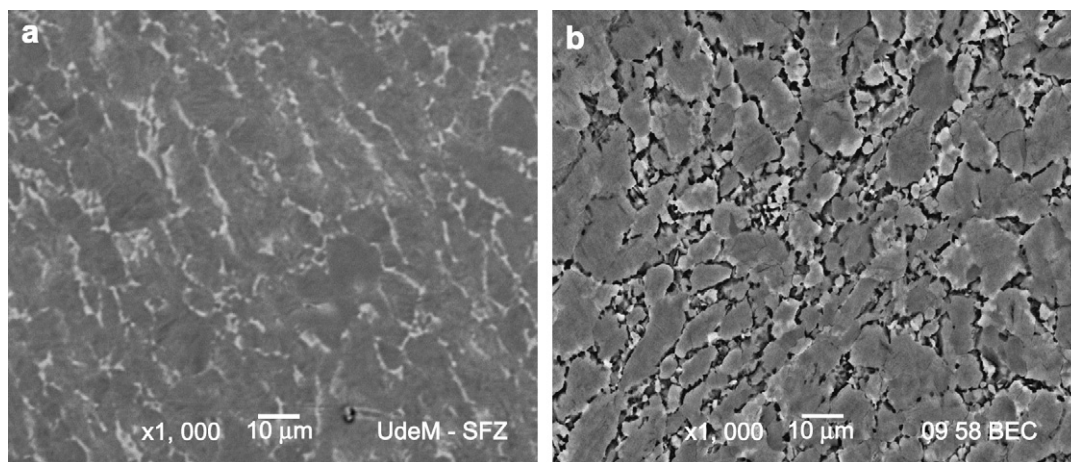


Fig. 1. (a) Backscattered SEM image of a polished untreated Ti-alloy disk. (b) Backscattered image of an etched alloy sample (4 h of exposure to the etching solution).

2.4.3. Raman spectroscopy

Raman spectroscopy (Renishaw Imaging Microscope Wire) was used to further characterize the surface oxide layer created on alloy disks, in order to determine their crystallographic structure and chemical composition at the molecular level. We used a green line laser (argon-ion excitation $\lambda = 514.5$ nm) at low intensities to avoid sample damage and modifications of the oxide properties due to laser heating.

2.4.4. Ellipsometry

Thickness of the oxide layer was estimated for each etching time from optical measurements using a variable-angle spectroscopic ellipsometer (VASE, J.A. Woollam Co., Inc.) and a double-beam spectrophotometer (Lambda 19, PerkinElmer) in the wavelength range 300–900 nm. Ellipsometric measurements were evaluated at two different angles of incidence (45° and 75°) with a 9.3-nm step for wavelength. Experimental data were fitted by using the Bruggeman equation for composite materials [44]. The graded layer was modelled as Ti substrate plus a second composite material made of a mixture of TiO_2 and voids.

2.5. Cell cultures

UMR-106 (CRL-1661, American Type Culture Collection, ATCC, Manassas, VA), osteoblast-like cells derived from rat, and NIH3T3 (CRL-1658, ATCC, VA), fibroblast-like cells derived from embryonic mouse, were routinely grown in Dulbecco's Modified Eagle Medium (DMEM, GIBCO®), 10% fetal calf serum (FCS, GIBCO®), 50 U/mL penicillin, and 50 U/mL streptomycin (Bio-Whittaker) in a 5% CO_2 and 95% air atmosphere at 37°C . A flask of cells were brought into suspension after incubating for 5 min in 0.5% trypsin (Bio-Whittaker). Following trypsinization, cells were washed by centrifugation at 500g for 5 min to give a pellet that was resuspended in 10 mL of fresh supplemented medium to a concentration of 10^4 cells/mL. Untreated disks and disks etched for 1 and 4 h were exposed for 24 h to UV light prior to use in cell culture experiments. They were placed in 24-well plates and 1 mL of the cell suspension was added to each well. The plated cells were cultured for 6 h and 3 days. Cell cultures were repeated twice with at least 10 samples for each condition.

2.6. Cell counting: optical counting and mitochondrial tetrazolium test (MTT)

Optical counting was performed to estimate cell number after 6 h of culture for both cell lines. The medium was removed and the samples were washed three times in phosphate-buffered saline (PBS, GIBCO®). Cells were fixed by adding 1 mL/well of paraformaldehyde (pH 7.2) for 15 min

at 25°C . Hoechst 33342 (Molecular Probes, Eugene, Oregon, USA), a nucleic acid stain often used as a substitute for DAPI, at 10 ng/mL was deposited in each well for 5 min to stain the nuclei. Samples were finally rinsed twice in PBS. The cell number was assessed by randomly taking pictures at $10\times$ with an epifluorescence microscope (Zeiss Axiophot) at 10 different zones along the surface of samples. Nuclei were counted on digital images using ImageTool (UTHSCSA). Optical counting was also done for NIH3T3 cells at 3 days in order to demonstrate correlation between microscopy and MTT readings (see below). Counts were not done on UMR-106 because this cell line has a rapid growth and cells pile-up at 3 days such that at this interval imaging provided no useful information for comparing cell number.

MTT was used to evaluate NIH3T3 and UMR-106 cell number after 3 days of culture. This is a common biochemical assay of cellular viability based on the reductive cleavage of yellow tetrazolium salt to a purple formazan compound by the dehydrogenase activity of intact mitochondria [45]. Consequently, this conversion only occurs in living cells. At the end of the culture interval, 100 μL of dye was added to the medium in each well. Samples (10

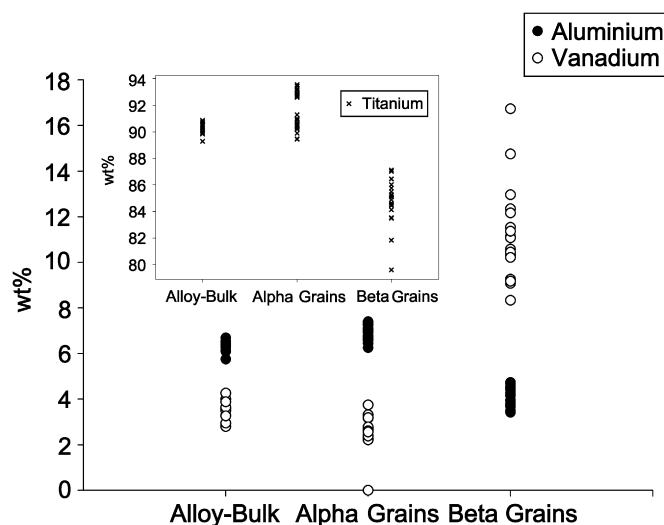


Fig. 2. Weight percentages (wt%) of Al, V, and Ti (inset) in bulk alloy, α -phase grains, and β -phase grains, as measured by EDX analysis of untreated disks at 15 kV.

per condition) were incubated at 37 °C for 4 h in a CO₂ incubator. The medium was gently aspirated and 300 µL of acidic propanol (500 mL propanol + 3.5 mL of 6 N aqueous HCl) was added to the culture plates, which were successively placed on a shaking platform for 2 h to ensure dissolution. Aliquots (150 µL) from each well were put into 96-well plates, and absorbance was measured in a multiplate reader (Biotek), using wavelengths of 550 nm and 620 nm. The absorbance difference ($A_{550\text{nm}} - A_{620\text{nm}}$) was calculated for each sample. The mean value obtained for cells on control disks was taken as a reference (100%).

2.7. Statistical analysis

Biological results were expressed as a mean value ± standard deviation for each sample. R software (The R Project for Statistical Computing, Vienna, Austria) was used to verify that data sets had a normal distribution in order to systematically compare all the conditions by pair with the *t*-test. For the 6 h counts, the data sets resulted as non-parametric and the Mann–Whitney rank sum test was used. In both cases, a *P* value of <0.05 was used to denote a significant difference.

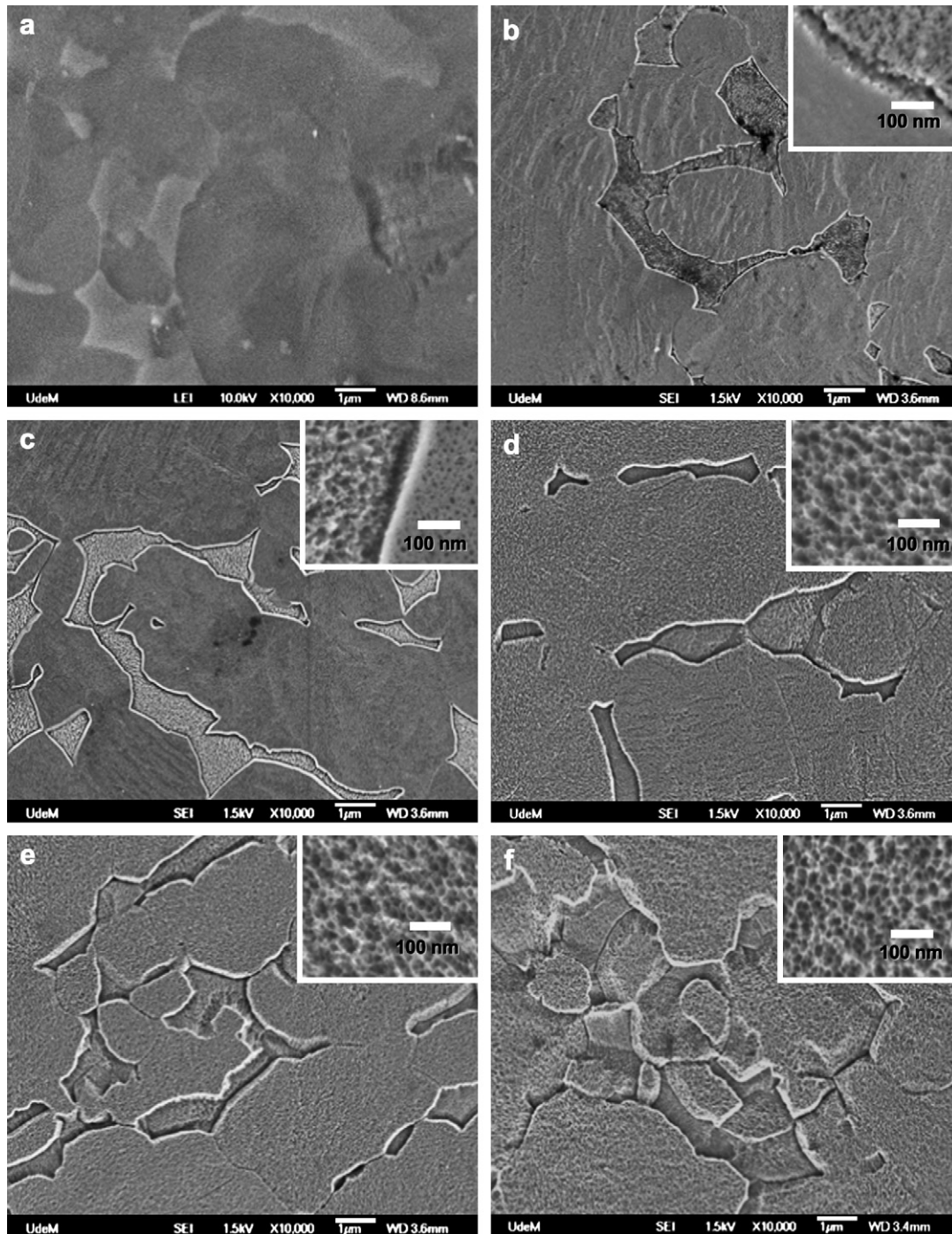


Fig. 3. SEM images (10,000×) of polished Ti-alloy disks. Image (a) corresponds to an untreated control, and images (b–f) show disks etched by piranha solution for 15 min, 30 min, 1 h, 2 h, and 4 h, respectively. Insets show nanotexture in high-resolution images (100,000×).

3. Results

3.1. Compositional and structural analysis

3.1.1. Scanning electron microscopy

To determine the distribution of the two phases (α and β) [2] present in Ti6Al4V, disks were imaged by SEM in back-scattered mode. The β -phase was initially present as interstitial grains surrounded by α -phase grains in untreated disks (Fig. 1a). In the course of etching, β -phase grains were preferentially removed and their presence decreased dramatically after 4 h (Fig. 1b), giving rise to a surface having a microscale texture characterized by cavities where β -phase grains were present initially. EDX analysis revealed differences in alloy composition and allowed the determination of the chemical compositions of the bulk and of α - and β -grains in control samples. Fig. 2 shows the weight percentages of Ti (inset), Al, and V in the bulk and in α - and β -grains. As anticipated, the β -phase is characterized by lower concentrations of Al and higher of V, confirming previous observations that V is a β -phase stabilizer [46,47]. By analyzing backscattered images with AnalySIS[®] software, we determined that β -grains occupy $8.4 \pm 3.1\%$ of the total surface of unetched disks.

SEM micrographs of the surfaces of Ti-alloy disks exposed to the etching solution for various times are displayed in Fig. 3. As the etching time increases, cavities corresponding to β -grains become more prominent, due to differences in the rate at which α - and β -grains are etched. High-resolution SEM imaging reveals more details of surfaces (Fig. 3 insets). Before chemical oxidation, the surfaces revealed no distinctive topographic features, aside from polishing grooves (Fig. 3a). In the case of samples etched for 15 min, the α -grains were still smooth at the nanoscale, but the β -grains had already developed nanotextured surfaces characterized by nanosized pits (Fig. 3b). After 30 min of etching (Fig. 3c), both α - and β -grains exhibited nanotextured surfaces. However, their morphologies were considerably different: isolated circular nanopits appeared on α -grains, and larger ellipsoidal nanopits were joined to one another on β -grains. Fig. 3d–f shows the effects of further etching and reveals that increasing oxidation time causes the nanoscale morphologies of α - and β -grains to become similar, with the entire surfaces covered by uniformly distributed nanopits and nanopeaks. Individual pits are not clearly distinguishable, because they are joined together to give rise to a three-dimensional sponge-like texture. By using AnalySIS[®] software, we obtained quantitative information about the evolution of pit growth on alloy surfaces. For this purpose, we considered only α -grains, which cover more than 90% of the total surface. Fig. 4 shows how the distribution of pit diameters varies with etching time. From such graphs, we infer that for longer etching times (1, 2, and 4 h), the number of pits with larger diameters increases. This presumably results from the joining of individual pits, giving rise to new nanocavities characterized by bigger diameters. After 15 and 30 min of etching, the mean pit diameter was about 13 ± 3 nm, and it reached 18 ± 6 nm, 21 ± 7 nm, and 20 ± 7 nm for 1, 2 and 4 h of etching, respectively.

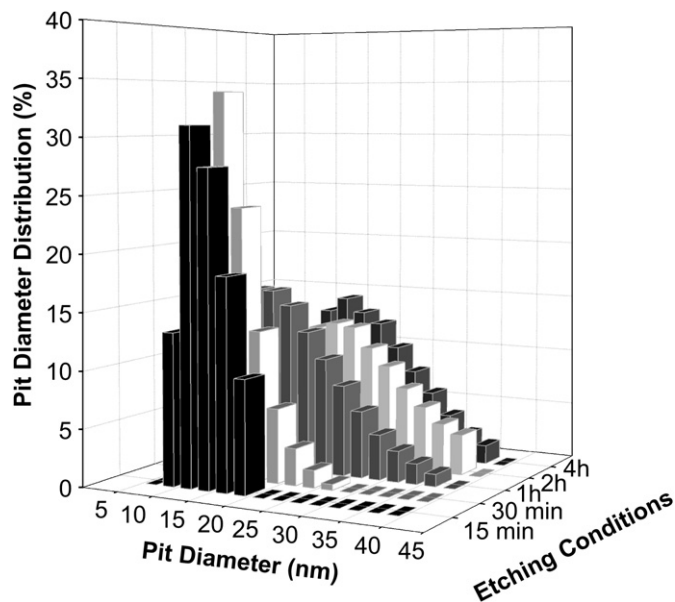


Fig. 4. Evolution of nanopit diameter as a function of etching time in α -phase grains. Measurements at 15 min refer to β -phase grains.

3.1.2. Atomic force microscopy

Fig. 5 shows how the surface topography of Ti-alloys changes with etching time. Chemical oxidation generates Ti6Al4V surfaces with both microtexture and nanotexture. As shown in Fig. 5a, the control sample is smooth on the nanoscale, and traces presumably related to mechanical polishing are the only features observed. Examination of Fig. 5b–f reveals the formation of a microtexture (formation of micro-size cavities corresponding to preferentially etched β -grains), as well as the appearance of nanotexture (increased surface roughness of both α - and β -grains).

Fig. 6a shows how the surface roughness of Ti-alloy (root-mean-square (RMS) roughness) changes with etching time. RMS values were measured only on α -grains, which cover more than 90% of the total surface. A clear trend was found: as expected from the AFM images, roughness at the nanoscale increased up to 2 h of treatment and thereafter remained unchanged. The observed values ranged from 3.8 ± 1.2 nm on unetched control samples to 11.6 ± 1.7 and 10.8 ± 2 nm on samples treated for 2 and 4 h, respectively. The AFM topographies also allowed us to measure the depth of microscale cavities resulting from disappearance of the more easily etched β -phase, which ranged from 11 ± 5 nm after 15 min of etching to 132 ± 25 nm and 178 ± 34 nm after 2 and 4 h, respectively (Fig. 6b).

3.2. Spectroscopic analysis

3.2.1. X-ray photoelectron spectroscopy (XPS)

High-resolution scans of Ti, Al, V, O, and C on selected samples, combined with peak deconvolution, allowed to determine the presence of different suboxides, such as TiO and Ti₂O₃, incorporated in the main oxide, which is composed mainly of TiO₂ and Al₂O₃. Fig. 7 shows the Ti_{2p} core-level

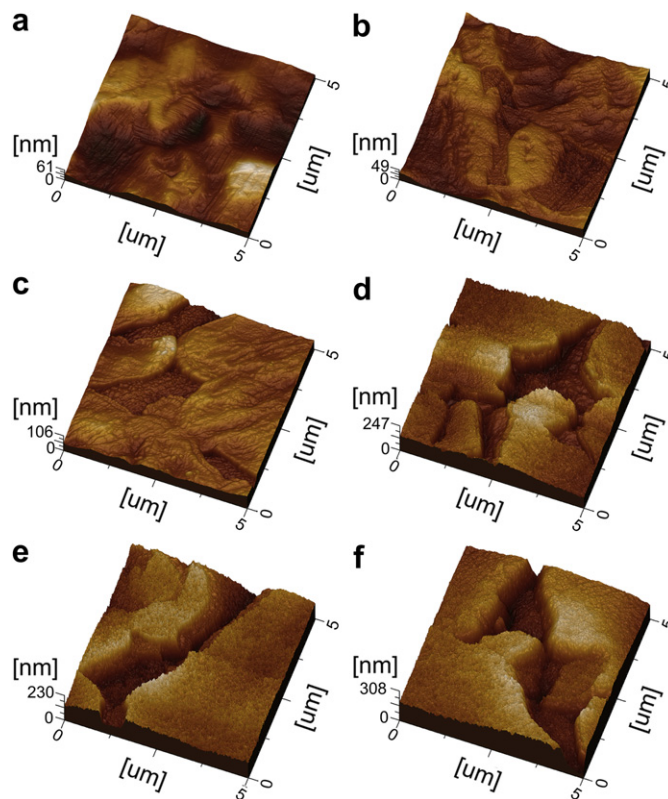


Fig. 5. AFM topographies ($5 \times 5 \mu\text{m}$) of polished Ti-alloy disks. Image (a) shows an untreated control, and images (b–f) correspond to surfaces exposed to piranha solution for 15 min, 30 min, 1 h, 2 h, and 4 h, respectively.

spectrum for an untreated control sample. A characteristic doublet appears at 458.8 and 464.3 eV, which has been attributed to Ti^{4+} , showing that TiO_2 is the main component of the surface. Deconvolution of the spectrum also revealed the presence of Ti^{3+} (457.4 and 464.2 eV), Ti^{2+} (455.7 and 460.2 eV), and $\text{Ti}^{\text{Metallic}}$ (454.1 and 460.3 eV), which presumably arise, respectively, from Ti_2O_3 , TiO , and the underlying metal [2,48–50]. The O_{1s} peak was deconvoluted by using three Gaussian–Lorentzian curves, which revealed the presence of Ti–O bonds (530.2 eV), OH^- groups (531.1 eV), and adsorbed H_2O (532.3 eV) [3,40,49,51]. Similarly, the C_{1s} peak was deconvoluted by using three Gaussian–Lorentzian curves located at 284.6, 286.2, and 288.5 eV, corresponding, respectively, to the binding energies of atoms involved in C–C, C–O, and C=O bonds. Finally, to determine surface composition, the following binding energies for Al and V have been considered: $\text{Al}_{2p_3}^{\text{Metallic}}$ at 72.9 eV, Al_{2p_3} (in the sapphire form of Al_2O_3) at 74.4 eV, $\text{V}_{2p_3}^{\text{Metallic}}$ at 512.2 eV, and V_{2p_3} (in V_2O_5) at 517.4 eV [50,52].

Table 1 reports the atomic concentrations of different oxides on surfaces of etched and untreated Ti-alloy disks. In all cases, TiO_2 proved to be the main surface oxide component, and its concentration did not vary significantly with etching time. TiO and Ti_2O_3 are present on the surface of control samples, but in much lower percentages than TiO_2 . The concentrations of both suboxides decreased with etching, and they could no longer be detected after 30 min of exposure to piranha solution.

On the other hand, the amount of Al_2O_3 increased initially with treatment time and reached the highest concentration after 1 h. Significant variations in the concentration of V_2O_5 were not detected in different samples. Finally, the $\text{Ti}^{\text{Metallic}}$ peak was not detected in samples treated for more than 15 min. XPS measurements also detected the presence of significant amounts of C, which were highest in samples etched for 2 h. XPS depth analysis revealed that the presence of C is mainly confined to the surface, since the intensity of the C_{1s} peak decreased to only about 5% of its original value after 300 s of plasma sputtering. By observing the evolution of the peak related to C with sputtering time (Fig. 8a), we noticed a double effect: the peak centered at 284.6 eV was no longer detected after 600 s of sputtering, and another peak centered at ~ 281 eV appeared for longer periods.

Fig. 8b displays the evolution of the Ti_{2p} peak as a function of sputtering time. Qualitatively, with increased time of sputtering, the characteristic doublet related to TiO_2 shifted towards lower binding energies through intermediate changes, until only the doublet relative to $\text{Ti}^{\text{Metallic}}$ was present, as previously described in the case of pure titanium [53–55].

3.2.2. Fourier transform infrared spectroscopy (FT-IR) and ellipsometry

Spectroscopic analysis by FT-IR showed that absorption in the $400\text{--}1000\text{ cm}^{-1}$ range changed with etching time. A broad two-component band has been associated with the amorphous

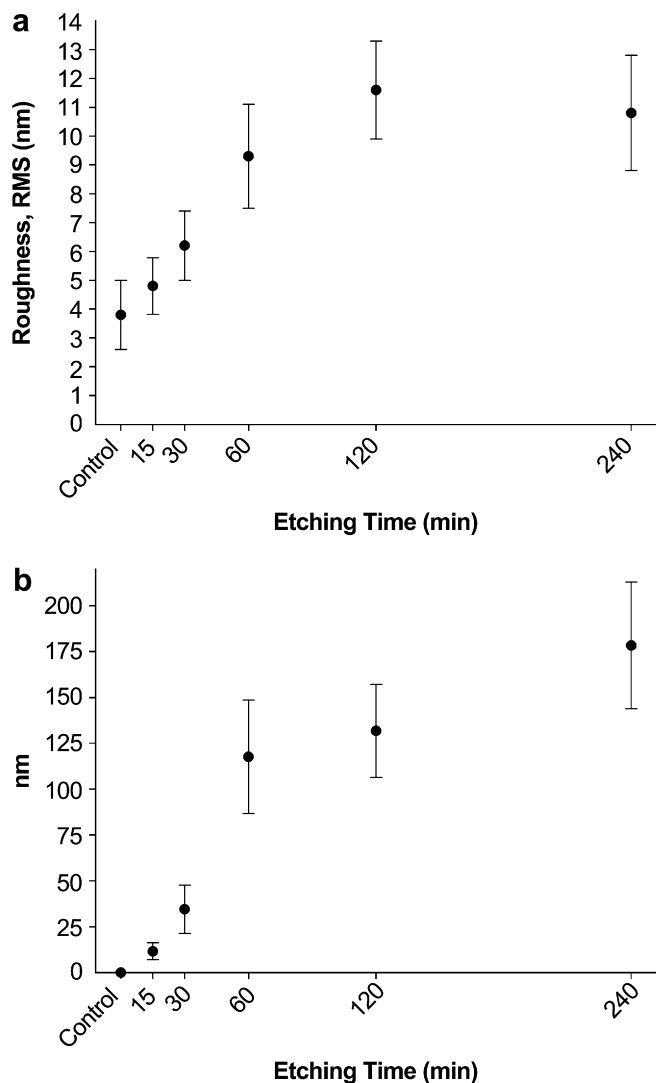


Fig. 6. (a) Graph showing how the roughness (RMS) of a Ti6Al4V surface changes as a function of etching time. RMS values were derived from AFM images ($1 \times 1 \mu\text{m}$) using WinSPM software. (b) Depth of micro-cavities resulting from etching of β -grains as a function of time.

state of TiO_2 [56,57], and it was possible to distinguish two bands located near 600 cm^{-1} and 800 cm^{-1} , which can be assigned to Ti–O stretching vibrations for Ti in tetrahedral and octahedral environments, respectively [58–62]. Fig. 9a shows the nature of these absorption peaks for etched disks and untreated controls. In untreated polished samples, peaks related to Ti–O bonds were very weak and broad, but absorbance increased in treated samples. To obtain a clearer assessment of this trend, we performed a quantitative analysis by using Pearson VII curves to fit the bands and by plotting the values of the total integrated area of Ti–O bands.

Fitting results were coupled with ellipsometric measurements, and they are displayed together on the same graph (Fig. 9b), which shows a close relation between the integrated area of IR peaks related to Ti–O bonds and the thickness of the oxide layer as estimated by ellipsometry. Such correlations between absorbance and oxide thickness were previously hypothesized by Trasferetti et al. [63] based on theoretical

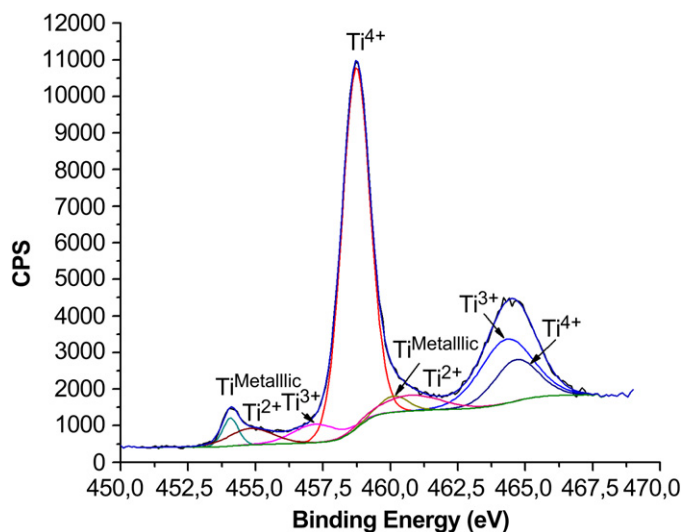


Fig. 7. High-resolution XPS spectra of Ti measured on the surface of an untreated Ti-alloy disk.

simulations. In agreement with these simulations, the oxide thickness measured by ellipsometry was about 5 nm in untreated samples, and it did not change significantly up to 15 min of etching (Fig. 9b). After 30 min of etching, however, oxide thickness increased steeply, reaching $\sim 45 \text{ nm}$ after 1 h of treatment. Samples etched for 2 and 4 h showed oxide layers with similar mean values of thickness (40–45 nm).

3.2.3. Raman spectroscopy and X-ray diffraction

Raman spectra collected on different samples had similar features (Fig. 10). No peak related to anatase or rutile was recorded in the $200\text{--}600 \text{ cm}^{-1}$ region [64], indicating that the surface oxide layer is mainly composed of amorphous TiO_2 , as also demonstrated by FT-IR analysis. This conclusion was supported by XRD measurements, which did not reveal the characteristic peak of either anatase or rutile in the $20\text{--}30^\circ$ range, respectively, at 25.281° and 27.507° [65] (Fig. 11 inset). Similarly, Raman spectra showed no significant peaks related to crystalline phases of Al_2O_3 and V_2O_5 [66]. Each spectrum presented a common feature: a sharp peak between 1500 and 1600 cm^{-1} , in the C–X stretching region (with X = C, N or O) [67,68].

3.3. Cell adhesion

The influence of treated surfaces on the initial cellular adhesion was determined by optically counting cell number after 6 h of culture. While adhesion of fibroblastic cells was not significantly influenced by treated surfaces, that of osteogenic cells on 4 h treated surfaces was about 25% lower (Fig. 12).

3.4. Cell proliferation

To assess the effect of our tailored Ti-alloy surfaces on cell proliferation, cell numbers were determined by the MTT technique. Osteoblastic cells showed a significantly higher number on treated surfaces compared with controls (Fig. 13).

Table 1
Dependence of the surface composition of a Ti6Al4V disk (wt%) as a function of etching time

	TiO ₂	TiO	Ti ₂ O ₃	Al ₂ O ₃	V ₂ O ₅	Ti ^{Metallic}	C
Control	16.2 ± 1.5	1.6 ± 0.4	0.7 ± 0.3	2.8 ± 0.6	0.5 ± 0.2	0.9 ± 0.2	20.5 ± 3.1
15 min	15 ± 1.3	2.1 ± 0.3	0.5 ± 0.3	2.7 ± 0.6	0.5 ± 0.2	1 ± 0.1	21.9 ± 1.8
30 min	16.8 ± 0.9	0.8 ± 0.2	0	3.1 ± 0.3	0.4 ± 0.2	0	22.3 ± 2.4
1 h	15.3 ± 1.6	0	0	3.9 ± 1.2	0.3 ± 0.2	0	22.4 ± 2.4
2 h	14.3 ± 1.6	0	0	3.6 ± 0.8	0.3 ± 0.2	0	28.2 ± 4.1
4 h	15.6 ± 0.8	0	0	3.6 ± 0.6	0.4 ± 0.2	0	25.1 ± 1.2

No statistical differences were found between the two conditions of etching. In the case of NIH3T3 cells (Fig. 13), the MTT method was coupled with optical counting of nuclei (Fig. 13 inset). Both techniques showed that treated surfaces

exhibit a significantly lower number of fibroblasts compared with unetched controls, and that cell numbers are similar in samples etched for 1 and 4 h. Observations by SEM of fibroblastic cultures after 3 days showed a major difference in surface coverage between controls (Fig. 14a) and treated surfaces (Fig. 14b,c). By using image analysis, we quantified these

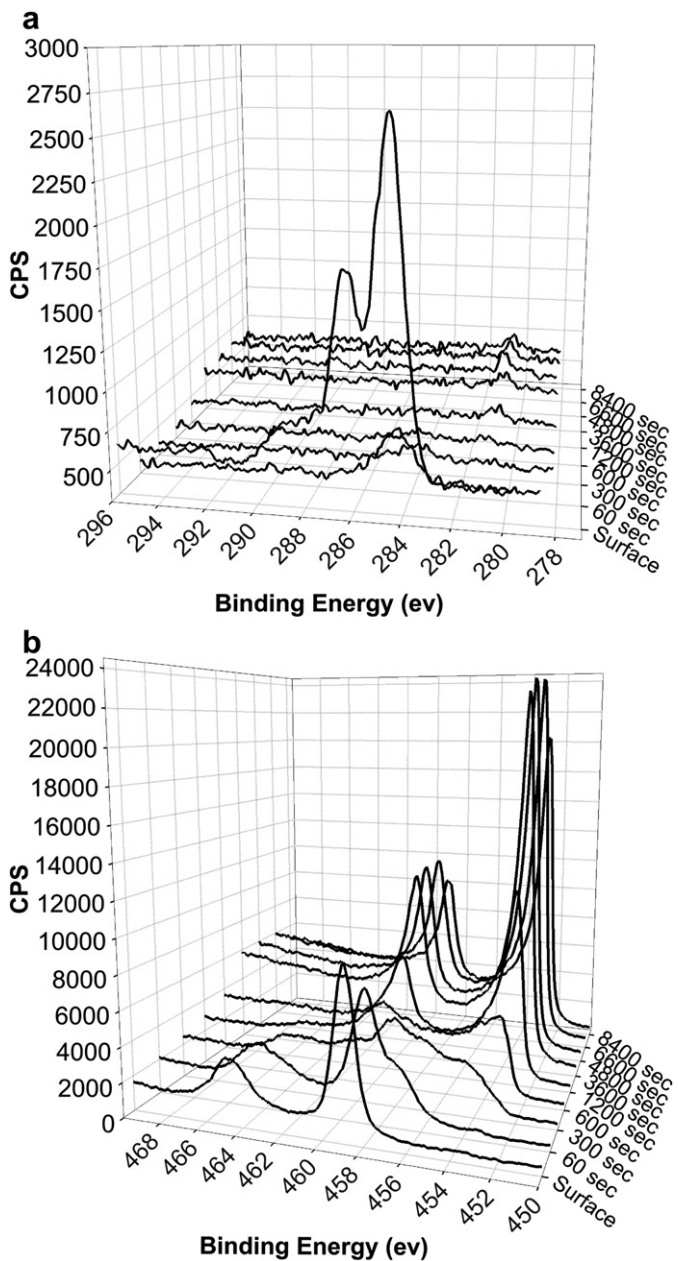


Fig. 8. XPS depth analyses of the evolution of (a) C_{1s} and (b) Ti_{2p} peaks with sputtering time.

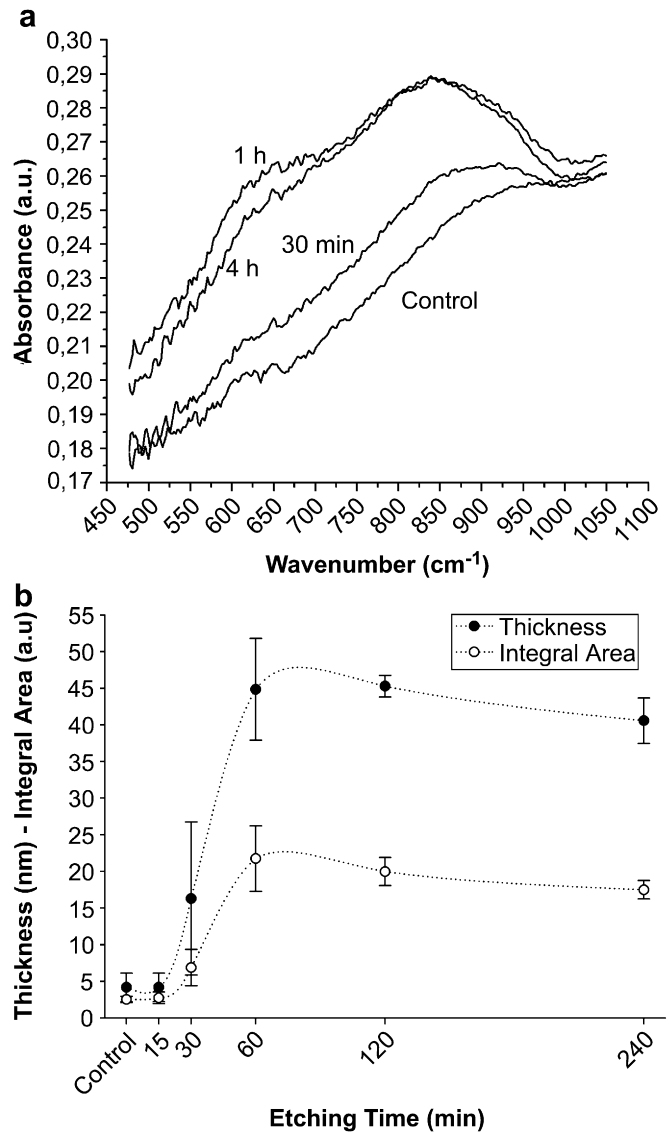


Fig. 9. (a) FT-IR spectra of etched Ti-alloy disks (30 min, 1 h, and 4 h of etching) and an untreated control in the region of Ti–O stretching. (b) Graph showing integrated Ti–O absorbance (FT-IR) and the thickness of the oxide layer (ellipsometry) as a function of etching time.

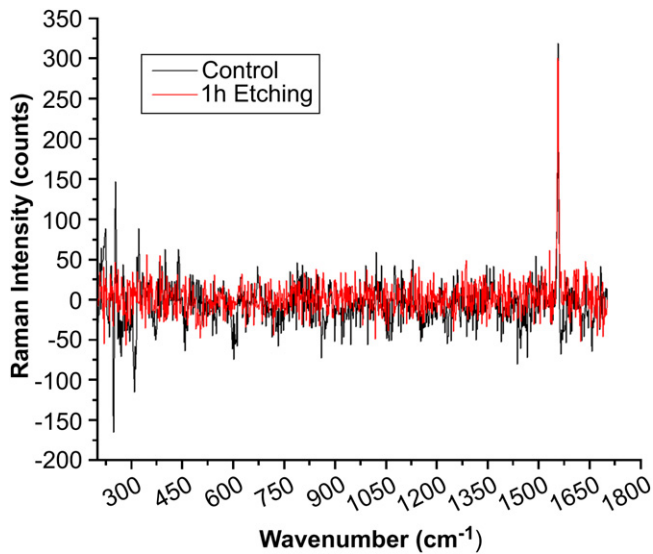


Fig. 10. Raman spectra of an untreated Ti-alloy disk and one exposed to piranha solution for 1 h.

differences in surface coverage and determined that NIH3T3 cells covered about 95% of the total surface of controls and about 55% of the surfaces of etched disks. High-resolution SEM images showed that cells spread into and over microtextured areas (Fig. 15a,b).

4. Discussion

Our work establishes that Ti6Al4V alloy can be nanotextured by simple oxidative treatment with a mixture of H₂SO₄/H₂O₂, and it has shown that the treatment time has an important influence on surface properties. The range of treatments we have applied generates a sponge-like texture consisting of

a network of nanopits similar to the one we have reported previously [30,40,41]. In addition, we have shown that the treatment can also generate microtexture in a single step by exploiting the intrinsic properties of the material. This is distinctive from previous reports where, in general, a combination of methods and/or coatings is used to achieve these two coexistent topographies, frequently on polymeric and semi-conductor materials [39,69,70]. Although the same oxidative mixture was used in earlier studies, the effect of treatment time was not evaluated nor were surface parameters examined in detail. In the present study, we report for the first time how treatment time affects various surface parameters such as nanoroughness and oxide thickness. We have also examined how changes in surface physicochemical characteristics and morphology of the disks induced by treatment collectively affect growth of osteogenic and fibroblastic cells in a differential manner.

β-Grains are attacked first and are more affected by the treatment, resulting in a difference in level between β- and α-grains and a consequential microtexture, which increases over time. Analysis by AFM, coupled with backscattered imaging and EDX analysis, allowed the formation of microtexture to be probed in detail. This analysis has suggested that a key element in the modification of the surface of Ti-alloys is the increased rate of etching of β-grains in Ti6Al4V alloy relative to α-grains, presumably because of the different electrochemical properties of the two phases. Our conclusion differs from that reached by Sittig et al. [2], who described the effects of treating Ti6Al4V with HNO₃/HF. In that case, α-grains were attacked more rapidly than β-grains. It is thought that such phenomena can be related to differences in electrochemical potential, with the β-phase being more anodic than the α-phase. This discrepancy may be due to the difference in both pH and the nature of the chemical oxidants, which thereby modify the kinetics and thermodynamics of the process.

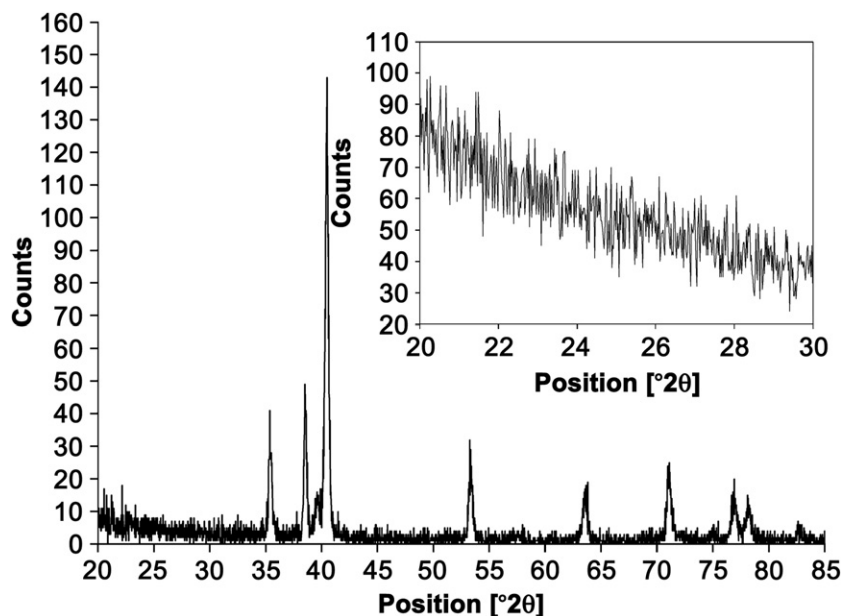


Fig. 11. Grazing-angle XRD pattern of a treated alloy surface (4 h). The inset displays XRD patterns in the 2θ range of 20–30°.

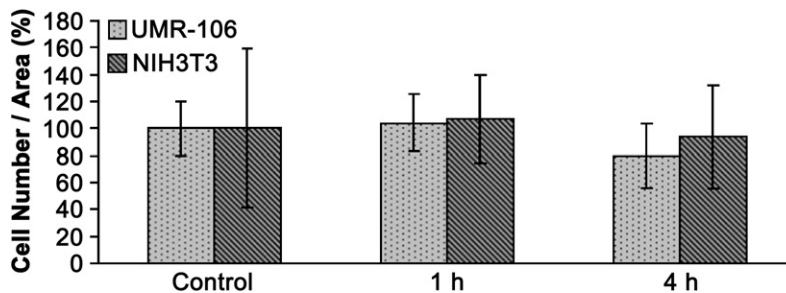


Fig. 12. Optical counting after 6 h of culture for UMR-106 osteoblastic and NIH3T3 fibroblastic cells.

SEM image analysis showed no significant increase in average diameter of nanopits with etching time; nevertheless, there is a significant evolution in their formation and structural organization. On both β - and α -grains, nanopits first appeared as isolated rounded cavities, which gradually overlap to acquire a more complex three-dimensional relationship. In addition to revealing morphological evolution at the microscale between β - and α -grains, our work has used AFM images to establish that nanoroughness increases with etching time. This provides further quantitative proof that surfaces are progressively modified, leading ultimately to the creation of porous three-dimensional sponge-like structures.

From spectroscopic investigations, we obtained valuable information about the crystallographic and physicochemical properties of the oxide layer created on the surface of the Ti-alloy. Both FT-IR and Raman spectroscopy showed that the layer is mainly amorphous. In particular, FT-IR spectra revealed bands characteristic of amorphous TiO_2 [56,57], and peaks related to crystalline phases were not clearly detected in Raman spectra. These findings, supplemented by XRD results, confirmed that our treatment creates a new oxide layer mainly composed of amorphous TiO_2 , as was previously found in the case of commercially pure Ti [40]. Both Raman spectroscopy and XPS analysis also revealed the presence of C on the surface. This signal does not derive from polishing, since non-polished samples showed even higher values

(~30%) than polished ones. As suggested by Nanci et al. [30], C likely originates from atmospheric sources resulting from storage of our samples in air; indeed, as shown by XPS depth analysis, the presence of C is mainly superficial. However, the fact that the C_{1s} peak shifted towards lower binding energies with increased sputtering time in the Ti–C bond region (~281 eV) [71] indicates that C is also present in low quantities in the bulk of the disks.

From FT-IR and ellipsometric analysis, we acquired quantitative information about changes in the thickness of the oxide layer as the etching time increased. The coupling of IR analysis with ellipsometric measurements demonstrated experimentally the growth of intensity in the IR band at $400\text{--}1000\text{ cm}^{-1}$ with increasing thickness of the TiO_2 layer, previously simulated by Trasferetti et al. [63]. Moreover, such an increase in the thickness of the oxide layer can be deduced from the failure to detect the XPS $\text{Ti}^{\text{Metallic}}$ peak after 15 min of etching. This is consistent with the fact that the ability of XPS to probe depth is limited to about 6 nm in the case of TiO_2 [2].

Analysis by XPS allowed us to monitor the chemical composition of the Ti-alloy surface as a function of etching time. This analysis established that the atomic concentration of the main constituent, TiO_2 , did not vary dramatically, but suboxides such as TiO and Ti_2O_3 were no longer detected in the main oxide layer after 30 min of etching. The superficial layer thus comprises a mixture of amorphous TiO_2 , Al_2O_3 , and

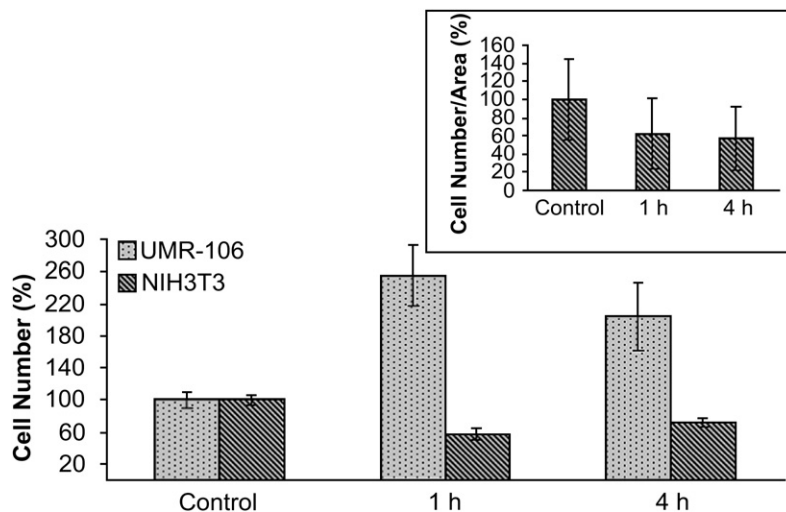


Fig. 13. MTT results for UMR-106 osteoblastic and NIH3T3 fibroblastic cells grown on etched Ti-alloy disks and untreated controls after 3 days. The inset provides counts for NIH3T3 using optical counting of nuclei.

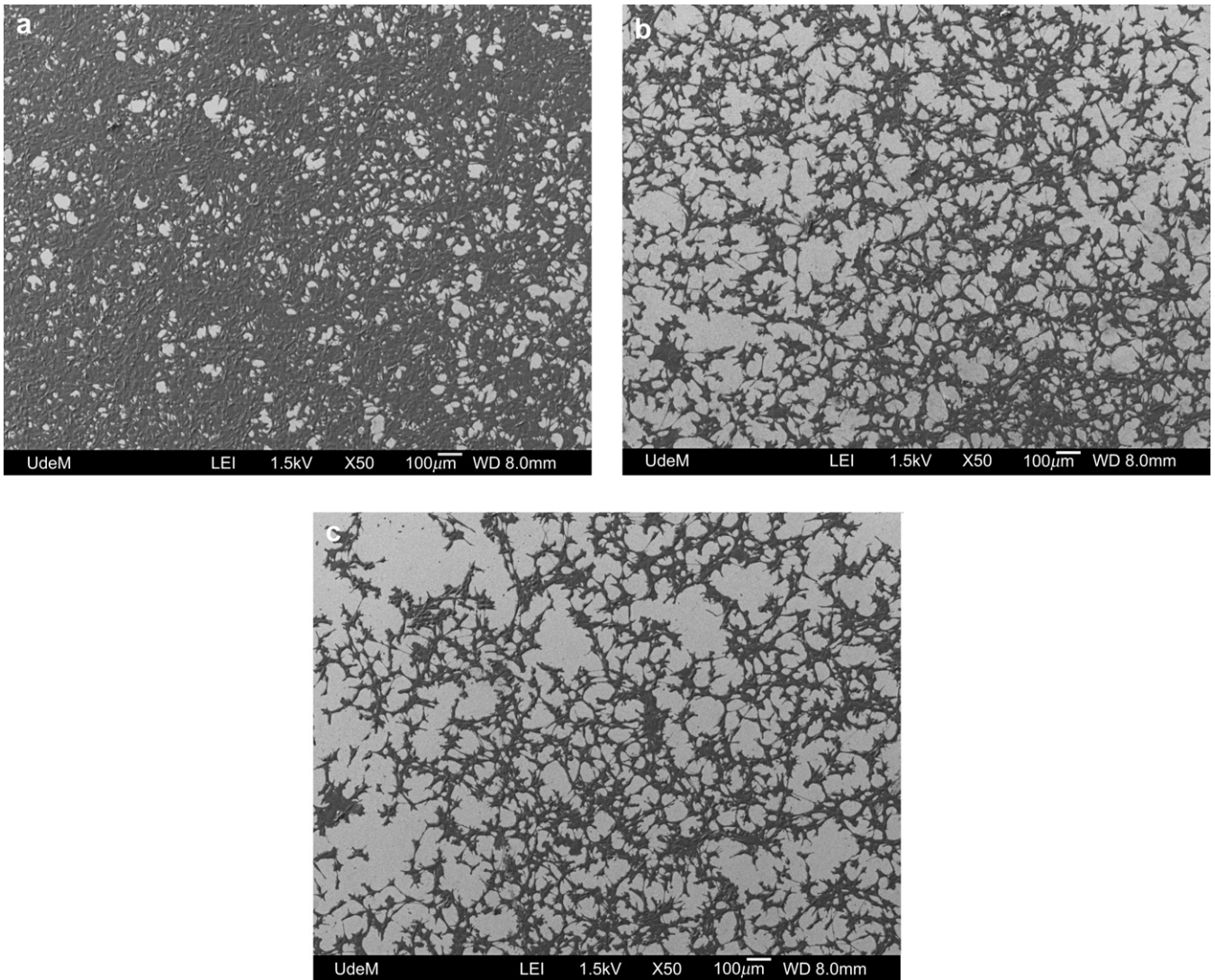


Fig. 14. SEM images of NIH3T3 fibroblasts grown on an untreated Ti-alloy control, on a disk etched for 1 h, and on a disk etched for 4 h (a–c, respectively).

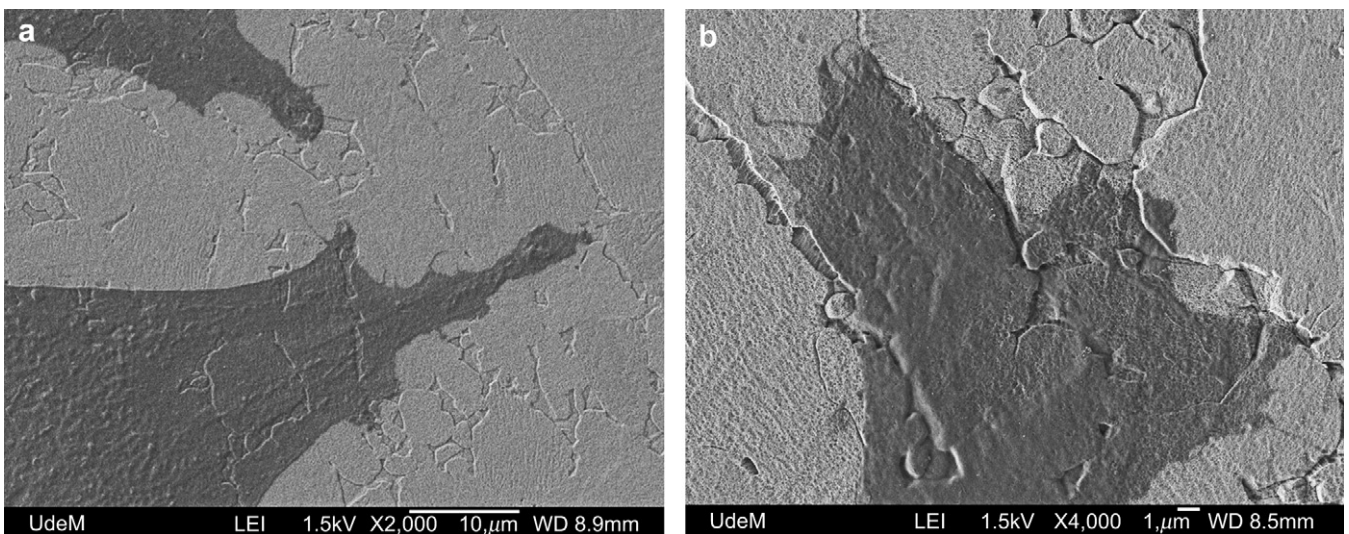


Fig. 15. SEM images of (a) UMR-106 and (b) NIH3T3 cells illustrating their relationship with microscale grooves resulting from preferential etching of β -grains.

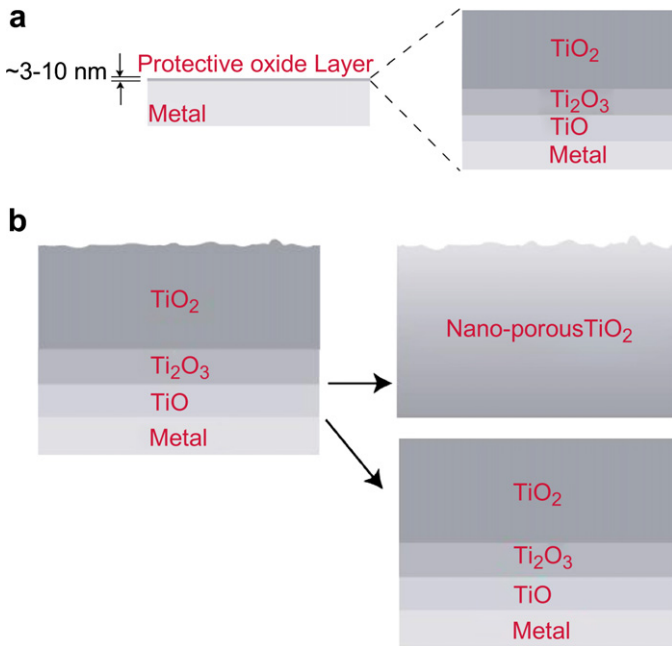


Fig. 16. Schematic representation of the layered structure (a) before (native oxide) and (b) after chemical oxidation.

small quantities of V_2O_5 after treatment. Because both surface and depth analyses by XPS showed the presence of suboxides below the surface of controls and samples treated for 4 h, our observations are consistent with the model for the oxide film proposed by McCafferty et al. [53], which is composed by three different layers, namely TiO (inner layer in contact with the metal), Ti_2O_3 (intermediate layer), and TiO_2 (outer layer) (Fig. 16a). In fact, the Ti_{2p} peak shift shown in Fig. 8b reflects this model; with increasing sputtering time, the Ti_{2p} doublet moved from binding energies characteristic of TiO_2 to those of Ti metal, through intermediate values that are assigned to suboxides [53–55]. These findings, coupled with IR and ellipsometric results, suggest that the oxidation process increases mainly TiO_2 to a degree that no longer allows detection of the underlying suboxides, but their layer organization is not altered. This behavior is chemically plausible and can be explained by assuming that suboxides such as TiO and Ti_2O_3 are transformed into TiO_2 in the oxidative medium of piranha solution [72], and by assuming that the etching solution penetrates the nanopits and reaches the underlying metal. When the solution reaches the suboxides, they are further oxidized into TiO_2 , thereby increasing the thickness of the dioxide layer in a manner consistent with ellipsometric measurements. When the underlying metal is exposed to the infiltrating solution, natural passivation conditions are recreated. This re-establishes the initial native layered structure, composed of TiO (in contact with the metal), Ti_2O_3 (intermediate), and TiO_2 (outer layer). However, now it is no longer in contact with the environment but rather with a nanoporous TiO_2 layer derived from suboxides transformation (Fig. 16b). Despite this porosity, the oxide thickness appears to reach a maximum value (~ 50 nm), possibly because (1) chemical reactions and fluid mobility may be altered by confinement

in nanoscale volumes or (2) at a critical thickness the rate of penetration of oxidant and the loss of material from the surface occur at similar rates and/or (3) the etching mixture may lose potency over time.

While increases in surface roughness and oxide thickness are known to affect cell activity [1,73,74], a critical finding that has emerged from this study is the discovery that nanoporous surfaces created by etching Ti-alloy can differentially influence cell activity. This effect favors the proliferation of osteoblastic cells (UMR-106) and limits that of fibroblastic cells (NIH3T3). There was no obvious effect on cell adhesion (seeding efficiency) except for osteoblastic cells grown on the 4 h treated surface which showed significantly less at 6 h of culture. After 3 days of culture, however, the UMR-106 cells ultimately catch up with the 1 h treated surface which shows significantly more cells than the control. While this observation is intriguing, it reaffirms the effect on cell proliferation and highlights the selective capacity of the nanoporous surface created by simple chemical oxidative patterning. Since the 1 and 4 h treated surfaces show essentially similar overall characteristics, the reason for the cellular differences observed at present can only be associated with the more profound etching of β -grains at 4 h. Since these grains occupy only about 8% of the surface and their dimensions are smaller than the cells, it is unlikely that the deeper etching has a direct effect on cell activity, particularly that UMR-106 and not NIH3T3 cells were affected. More specifically, the dimensions of the features caused by the preferential dissolution of β -grains do not provide any differential signaling cues because cells are large enough to spread across them. It may, however, affect such initial parameters as wettability and protein self-adsorption, well-known to affect cell adhesion [75,76]. Later, it would appear that surface physicochemical parameters such as oxide thickness, chemical composition, and pit size are more determinant. Since increasing treatment time from 1 to 4 h is not sufficient to induce major changes in these parameters, then no significant difference in cell growth results.

In a study using another titanium alloy and where sulfuric acid was used for anodization [77], it was demonstrated that selective etching of grains as we have shown and nanoscale surface modifications do not affect the mechanical properties of the material. In fact, in this study, the authors actually showed that the treatment improved fatigue strength.

5. Conclusions

Our work has established the feasibility of creating bioactive nano- and microtextured surfaces on Ti6Al4V alloy by simple treatment with H_2SO_4/H_2O_2 . The physicochemical characteristics of these surfaces can be tailored by controlling the duration of etching. Other variables, including temperature and the concentration and nature of the etching agents, may further alter surface properties in a controlled manner and are the subject of ongoing studies in our group. In addition, we have demonstrated that textured Ti-alloy surfaces have a selective effect on cells, as revealed by facilitated growth of osteogenic cells and limited growth of fibroblastic cells. This differential effect

is critical for successful dental and orthopedic implants, which depend not only on forming bone but also on limiting detrimental fibrous encapsulation [78,79]. Our results suggest that the nanoporous oxidized Ti-alloy surfaces that we have generated can provide cues to cells that engender specific cellular responses. Identification of the molecular mechanisms involved and their correlation with specific surface characteristics may lead to the rational design of novel biomaterials with “intelligent surfaces” capable of eliciting optimal healing responses in host tissues. Healing time can be reduced, and the functionality and stability of implants may no longer be compromised by the creation of soft tissue at the interface with the host [80].

Acknowledgments

We thank R. Vernhes for his help in obtaining ellipsometric measurements. We are also grateful to C. Chabanier and G. Veilleux for sharing their experience and helpful advice about the collection and analysis of XPS data, S. Francis Zalzal for her assistance with SEM, and K. Sellin for cell cultures, and to F. Vetrone for critical reading of the manuscript. In addition, F.V. acknowledges the Canadian Bureau for International Education (CBIE) and FQRNT (Fonds Québécois de la Recherche sur la Nature et les Technologies) for financial support. This work was supported by NSERC (Natural Sciences and Engineering Research Council of Canada) and CIHR (Canadian Institutes of Health Research). J.D.W. and F.R. acknowledge additional support from FQRNT and the CRC (Canada Research Chairs) program. A.N. and F.R. are grateful to NSERC for support through a Collaborative Research and Development (CRD) program with Plasmionique Inc. Infrastructure support from the CFI (Canadian Foundation for Innovation) is also acknowledged.

References

- [1] Zhu X, Chen J, Scheideler L, Reichl R, Geis-Gerstorfer J. Effects of topography and composition of titanium surface oxides on osteoblast responses. *Biomaterials* 2004;25:4087–103.
- [2] Sittig C, Textor M, Spencer ND, Wieland M, Vallotton P-H. Surface characterization of implant materials c.p.Ti, Ti-6Al-7Nb and Ti-6Al-4V with different pretreatments. *J Mater Sci Mater Med* 1999;10:35–46.
- [3] Feng B, Weng J, Yang BC, Qu SX, Zhang XD. Characterization of surface oxide films on titanium and adhesion of osteoblast. *Biomaterials* 2003;24:4663–70.
- [4] Feng B, Weng J, Yang BC, Chen JY, Zhao JZ, He L, et al. Surface characterization of titanium and adsorption of bovine serum albumin. *Mater Charact* 2003;49:129–37.
- [5] Oh H-J, Lee J-H, Jeong Y, Kim Y-J, Chi C-S. Microstructural characterization of biomedical titanium oxide film fabricated by electrochemical method. *Surf Coat Technol* 2005;198:247–52.
- [6] Brunski JB, Puleo DA, Nanci A. Biomaterials and biomechanics of oral and maxillofacial implants: current status and future developments. *Int J Oral Maxillofac Implants* 2000;15:15.
- [7] Anselme K, Bigerelle M. Statistical demonstration of the relative effect of surface chemistry and roughness on human osteoblast short-term adhesion. *J Mater Sci Mater Med* 2006;17:471–9.
- [8] Refai A, Textor M, Brunette D, Waterfield J. Effect of titanium surface topography on macrophage activation and secretion of proinflammatory cytokines and chemokines. *J Biomed Mater Res* 2004;70A:194–205.
- [9] Guizzardi S, Galli C, Martini D, Belletti S, Tinti A, Raspanti M, et al. Different titanium surface treatment influences human mandibular osteoblast response. *J Periodontol* 2004;75(2):273–82.
- [10] Luthen F, Lange R, Becker P, Rychly J, Beck U, Nebe JGB. The influence of surface roughness of titanium on β 1- and β 3-integrin adhesion and the organization of fibronectin in human osteoblastic cells. *Biomaterials* 2005;26:2423–40.
- [11] Cassinelli C, Morra M, Bruzzone G, Carpi A, Santi GD, Giardino R, et al. Surface chemistry effects of topography modification of titanium dental implant surfaces: 2 in vitro experiments. *Int J Oral Maxillofac Implants* 2003;18(1):46–52.
- [12] Xavier S, Carvalho P, Beloti M, Rosa A. Response of rat bone marrow cells to commercially pure titanium submitted to different surface treatments. *J Dent* 2003;31:173–80.
- [13] Zhao G, Zinger O, Schwartz Z, Wieland M, Landolt D, Boyan BD. Osteoblast-like cells are sensitive to submicron-scale surface structure. *Clin Oral Implants Res* 2006;17(3):258–64.
- [14] Das K, Bose S, Bandyopadhyay A. Surface modification and cell–materials interactions with anodized Ti. *Acta Biomater* 2007.
- [15] Dalby MJ, McCloy D, Robertson M, Wilkinson CDW, Oreffo ROC. Osteoprogenitor response to defined topographies with nanoscale depths. *Biomaterials* 2006;27:1306–15.
- [16] Andersson A, Brink J, Lidberg U, Sutherland D. Influence of systematically varied topography on the morphology of epithelial cells. *IEEE Trans Nanobiosc* 2003;2(2):49–57.
- [17] Ismail F, Rohanizadeh R, Atwa S, Mason R, Ruys A, Martin P, et al. The influence of surface chemistry and topography on the contact guidance of MG63 osteoblast cells. *J Mater Sci Mater Med* 2006;18(5):705–14.
- [18] Liu X, Chu PK, Ding C. Surface modification of titanium, titanium alloys, and related materials for biomedical applications. *Mater Sci Eng R* 2004;47:49–121.
- [19] Nayab S, Jones F, Olsen I. Effects of calcium ion implantation on human bone cell interaction with titanium. *Biomaterials* 2005;26:4717–27.
- [20] Krupa D, Baszkiewicz J, Kozubowski J, Barcz A, Sobczak J, Biliniski A. Effect of calcium-ion implantation on the corrosion resistance and biocompatibility of titanium. *Biomaterials* 2001;22:2139–51.
- [21] Nayab S, Jones F, Olsen I. Human alveolar bone cell adhesion and growth on ion implanted titanium. *J Biomed Mater Res* 2004;69A:651–7.
- [22] Anselme K, Bigerelle M. Topography effects of pure titanium substrates on human osteoblast long-term adhesion. *Acta Biomater* 2005;1(2):211–22.
- [23] Giordano C, Sandrini E, Busini V, Chiesa R, Fumagalli G, Giavaresi G, et al. A new chemical etching process to improve endosseous implant osseointegration: in vitro evaluation on human osteoblast-like cells. *Int J Artif Organs* 2006;29(8):772–80.
- [24] Mandrini E, Giordano C, Busini V, Signorelli E, Cigada A. Apatite formation and cellular response of a novel bioactive titanium. *J Mater Sci Mater Med* 2006;18(6):1225–37.
- [25] Anselme K, Bigerelle M, Noel B, Iost A, Hardouin P. Effect of grooved titanium substratum on human osteoblastic cell growth. *J Biomed Mater Res* 2002;60:529–40.
- [26] Lincks J, Boyan BD, Blanchard CR, Lohmann CH, Liu Y, Cochran DL, et al. Response of MG63 osteoblast-like cells to titanium and titanium alloy is dependent on surface roughness and composition. *Biomaterials* 1998;19:2219–32.
- [27] Linez-Bataillon P, Monchau F, Bigerelle M, Hildebrand HF. In vitro MC3T3 osteoblast adhesion with respect to surface roughness of Ti6Al4V substrates. *Biomol Eng* 2002;19:133–41.
- [28] Rupp F, Scheideler L, Rehbein D, Axmann D, Geis-Gerstorfer J. Roughness induced dynamic changes of wettability of acid etched titanium implant modifications. *Biomaterials* 2004;25:1429–38.
- [29] de Oliveira PT, Zalzal SF, Irie K, Nanci A. Early expression of bone matrix proteins in osteogenic cell cultures. *J Histochem Cytochem* 2003;51(5):633–41.
- [30] Nanci A, Wuest JD, Peru L, Brunet P, Sharma V, Zalzal S, et al. Chemical modification of titanium surfaces for covalent attachment of biological molecules. *J Biomed Mater Res* 1998;40:324–35.
- [31] Ergun C, Liu H, Halloran JW, Webster TJ. Increased osteoblast adhesion on nanograned hydroxyapatite and tricalcium phosphate containing calcium titanate. *J Biomed Mater Res* 2007;80A:990–7.

- [32] Zhu X, Eibl O, Scheideler L, Geis-Gerstorf J. Characterization of nano hydroxyapatite/collagen surfaces and cellular behaviors. *J Biomed Mater Res* 2006;79A:114–27.
- [33] Meyer U, Büchter A, Wiesmann HP, Joos U, Jones DB. Basic reaction of osteoblasts on structured material surfaces. *Eur Cell Mater* 2005;9:39–49.
- [34] Li P. Biomimetic nano-apatite coating capable of promoting bone ingrowth. *J Biomed Mater Res* 2003;66A:79–85.
- [35] Ball MD, Prendergast U, O'Connell C, Sherlock R. Comparison of cell interactions with laser machined micron- and nanoscale features in polymer. *Exp Mol Pathol* 2007;82:130–4.
- [36] Teixeira AI, McKie GA, Foley JD, Bertics PJ, Nealey PF, Murphy CJ. The effect of environmental factors on the response of human corneal epithelial cells to nanoscale substrate topography. *Biomaterials* 2006;27:3945–54.
- [37] Diehl KA, Foley JD, Nealey PF, Murphy CJ. Nanoscale topography modulates corneal epithelial cell migration. *J Biomed Mater Res* 2005;75A:603–11.
- [38] Barbucci R, Pasqui D, Wirsen A, Affrossman S, Curtis A, Tetta C. Micro and nano-structured surfaces. *J Mater Sci Mater Med* 2003;14:721–5.
- [39] Wan Y, Wang Y, Liu Z, Qu X, Han B, Bei J, et al. Adhesion and proliferation of OCT-1 osteoblast-like cells on micro- and nano-scale topography structured poly(L-lactide). *Biomaterials* 2005;26:4453–9.
- [40] Yi J-H, Bernard C, Variola F, Zalzal SF, Wuest JD, Rosei F, et al. Characterization of a bioactive nanotextured surface created by controlled chemical oxidation of titanium. *Surf Sci* 2006;600:4613–21.
- [41] de Oliveira PT, Nanci A. Nanotexturing of titanium-based surfaces upregulates expression of bone sialoprotein and osteopontin by cultured osteogenic cells. *Biomaterials* 2004;25:403–13.
- [42] de Oliveira PT, Zalzal SF, Beloti MM, Rosa AL, Nanci A. Enhancement of *in vitro* osteogenesis on titanium by chemically produced nanotopography. *J Biomed Mater Res* 2007;80A:554–64.
- [43] Adem E. XPS and Auger Handbook. FISON'S Instruments Surface Science.
- [44] Vernhes R, Amassian A, Klemborg-Sapieha JE, Martinu L. Plasma treatment of porous SiN_x: H films for the fabrication of porous-dense multilayer optical filters with tailored interfaces. *J Appl Phys* 2006;99:114315.
- [45] Denizot F, Lang R. Rapid colorimetric assay for cell growth and survival: modifications to the tetrazolium dye procedure giving improved sensitivity and reliability. *J Immunol Methods* 1986;89:271–7.
- [46] Soboyejo WO, Nemetski B, Allameh S, Marcantonio N, Mercer C, Ricci J. Interactions between MC3T3-E1 cells and textured Ti6Al4V surfaces. *J Biomed Mater Res* 2002;62:57–72.
- [47] Fan Z, Miodownik AP. TEM study of metastable β -phase decomposition in rapidly solidified Ti-6Al-4V alloy. *J Mater Sci* 1994;29:6403–12.
- [48] Lee TM, Chang E, Yang CY. Surface characteristics of Ti6Al4V alloy: effect of materials, passivation and autoclaving. *J Mater Sci Mater Med* 1998;9:439–48.
- [49] Pouilleau J, Devilliers D, Garrido F, Durand-Vidal S, Mahé E. Structure and composition of passive titanium oxide films. *Mater Sci Eng B* 1997;47:235–43.
- [50] PerkinElmer. Handbook of X-ray photoelectron spectroscopy; 1992.
- [51] Zhang W, Li Y, Zhu S, Wang F. Influence of argon flow rate on TiO₂ photocatalyst film deposited by dc reactive magnetron sputtering. *Surf Coat Technol* 2004;182:192–8.
- [52] Cai K, Bossert J, Jandt KD. Does the nanometre scale topography of titanium influence protein adsorption and cell proliferation? *Colloids Surf B* 2006;49:136–44.
- [53] McCafferty E, Wightman JP. An X-ray photoelectron spectroscopy sputter profile study of the native air-formed oxide film on titanium. *Appl Surf Sci* 1999;143:92–100.
- [54] Lisowski W, van den Berg AHJ, Smithers M. Characterization of titanium hydride film after long-term air interaction: SEM, ARXPS and AES depth profile studies. *Surf Interface Anal* 1998;26:213–9.
- [55] Arys A, Philippart C, Douvrou N, He Y, Le QT, Pireaux JJ. Analysis of titanium dental implants after failure of osseointegration: combined histological, electron microscopy, and X-ray photoelectron spectroscopy approach. *J Biomed Mater Res* 1998;43:300–12.
- [56] Viitala RI, Langlet M, Simola J, Linden M, Rosenholm JB. Aerosol-gel deposition of doped titania thin films. *Thin Solid Films* 2000;368:35–40.
- [57] Amor SB, Baud G, Besse JP, Jacquet M. Structural and optical properties of sputtered titania films. *Mater Sci Eng B* 1997;47:110–8.
- [58] Velten D, Biehl V, Aubertin F, Valeske B, Possart W, Breme J. Preparation of TiO₂ layers on cp-Ti and Ti6Al4V by thermal and anodic oxidation and by sol-gel coating techniques and their characterization. *J Biomed Mater Res* 2002;59:18–28.
- [59] Amor SB, Guedri L, Baud G, Jacquet M, Ghedira M. Influence of the temperature on the properties of sputtered titanium oxide films. *Mater Chem Phys* 2002;77:903–11.
- [60] Castañeda L, Alonso JC, Ortiz A, Andrade E, Saniger JM, Bañuelos JG. Spray pyrolysis deposition and characterization of titanium oxide thin films. *Mater Chem Phys* 2002;77:938–44.
- [61] Lopez T, Moreno J, Gomez R, Bokhimi X, Wang JA, Yee-Madeira H, et al. Characterization of iron-doped titania sol-gel materials. *J Mater Chem* 2002;12:714–8.
- [62] Urlaub R, Posset U, Thull R. FT-IR spectroscopic investigations on sol-gel-derived coatings on acid-modified titanium alkoxides. *J Non-Cryst Solids* 2000;265:276–84.
- [63] Transferetti BC, Davanzo CU, Zoppi RA, da Cruz NC, de Moraes MAB. Berreman effect applied to phase characterization of thin films supported on metallic substrates: the case of TiO₂. *Phys Rev B* 2001;64:125404.
- [64] Furic K, Stoch L, Dutkiewicz J. Raman study of TiO₂ role in SiO₂-Al₂O₃-MgO-TiO₂-ZnO glass crystallization. *Spectrochim Acta A* 2005;61:1653–9.
- [65] XRD Joint Committee on Powder Diffraction Standards (JCPDS) data file No. 44–1294.
- [66] Tian H, Ross EI, Wachs IE. Quantitative determination of the speciation of surface vanadium oxides and their catalytic activity. *J Phys Chem B* 2006;110:9593–600.
- [67] Kodati VR, Tu AT, Turumin JL. Raman spectroscopic identification of uric-acid-type kidney stone. *Appl Spectrosc* 1990;44(7):1134–6.
- [68] Klubovich VV, Khamchukov YD, Egorov VD. Raman spectra of carbon coatings on a metal alloy. *J Appl Spectrosc* 1993;59:523–7.
- [69] Flemming RG, Murphy CJ, Abrams GA, Goodman SL, Nealey. Effects of synthetic micro and nano-structured surfaces on cell behaviour. *Biomaterials* 1999;20:573–88.
- [70] Gadegaard N, Martinez E, Riehle MO, Seunarine K, Wilkinson CDW. Applications of nano-patterning to tissue engineering. *Microelectron Eng* 2006;83:1577–81.
- [71] Cardinaud CH, Lemperiere G, Peignon MC, Jouan PY. Characterisation of TiN coatings and of TiN/Si interface by X-ray photoelectron spectroscopy and Auger electron spectroscopy. *Appl Surf Sci* 1993;68:595–603.
- [72] Hanawa T, Asami K, Asaoka K. Repassivation of titanium and surface oxide film regenerated in simulated body fluid. *J Biomed Mater Res* 1998;40:530–8.
- [73] Saldana L, Barranco V, Gonzalez-Carrasco JL, Rodriguez M, Munuera L, Vilaboa N. Thermal oxidation enhances early interactions between human osteoblasts and alumina blasted Ti6Al4V alloy. *J Biomed Mater Res A* 2007;81:334–46.
- [74] Muhonen V, Heikkinen R, Danilov A, Jamsa T, Tuukkanen J. The effects of oxide thickness on osteoblast attachment and survival on NiTi alloy. *J Mater Sci Mater Med* 2007;18:959–67.
- [75] Kasemo B. Biological surface science. *Surf Sci* 2002;500(1):656–77.
- [76] Anselme K. Osteoblast adhesion on biomaterials. *Biomaterials* 2000;21:667–81.
- [77] Leinenbach C, Eifler D. Fatigue and cyclic deformation behaviour of surface-modified titanium alloys in simulated physiological media. *Biomaterials* 2006;27:1200–8.
- [78] Frenkel SR, Simon J, Alexander H, Dennis M, Ricci JL. Osseointegration on metallic implant surfaces: effects of microgeometry and growth factor treatment. *J Biomed Mater Res* 2002;63:706–13.
- [79] Thomsen P, Gretzer C. Macrophage interactions with modified material surfaces. *Curr Opin Solid State Mater Sci* 2001;5:163–76.
- [80] Anderson JM. Biological responses to materials. *Annu Rev Mater Res* 2001;31:81–110.